DOI: 10.1002/adma.200502263

Building Nanocrystalline Planar Defects within Self-Assembled Photonic Crystals by Spin-Coating**

By *Raúl Pozas, Agustín Mihi, Manuel Ocaña, and Hernán Míguez**

The development of techniques to introduce defects within photonic crystals in a controlled manner has attracted great interest since the early days of the field.[1] This attention is due to the potential technological applications resulting from the optical properties associated with defect state modes carefully engineered into the photonic gap of such lattice structures.[2] In spite of the great focus on this field, only very recently has this interest been extended to solid, self-assembled, colloidal photonic crystals. The reason behind this delay is the high density of intrinsic defects present in the early crystals made by self-assembly.[3] Thus, in the past much effort was focused on getting rid of such unwanted defects rather than on introducing new ones.

However, since the introduction of the vertical deposition technique by Colvin and co-workers,[4] and the subsequent development of different variations of this method,[5,6] this picture has largely changed. Nowadays, planar colloidal crystals with high optical quality can be fabricated on a wide variety of substrates,[7] allowing control over both orientation and crystal size. The improvement in the quality of self-assembled photonic crystals has motivated preliminary experimental work on the controlled introduction of defects in artificial opals. Buried polymer defect lines in a silica opal were first achieved by using a multiphoton confocal laser to selectively induce polymerization of an embedded monomer.[8] Afterwards, different motifs have been drawn or built within colloidal crystals by a wide variety of techniques, including direct laser writing,[9] electron-beam lithography,[10,11] photolithography,[12,13] or by modifications of the originally proposed method.[14]

Regarding planar defects, a few successful approaches have been developed up to now. A layer of spheres of an arbitrary diameter can be introduced into the bulk of an opal by combining colloidal-crystal planarization and Langmuir–Blodgett techniques.[15] A combination of convective self-assembly and chemical vapor deposition (CVD) has been used to create a silicon oxide slab sandwiched between two opal films.[16,17] In this approach, the starting opal film has to be infiltrated with a guest compound until the entrance pores are closed,[18] thus allowing the deposition of a coating of the desired thickness on the lattice surface. Afterwards, a new colloidal crystal is formed on top of the coating and also infiltrated in order to present a similar composition to the starting opal. A transfer-printing technique has also been successfully employed to place a polymer multilayer of controlled thickness on top of an opal film, followed by the subsequent growth of a second opal layer.[19] The optical effects associated with the presence of defects, such as sharp dips (peaks) in the reflectance (transmittance) spectra at stop band frequencies, are stronger for the latter case than for the previous examples. The reason for this is that transfer printing permits polymer defect layers to be constructed without infiltrating the surrounding opal films, unlike CVD processes used to grow oxide planar defects, which largely diminish the photonic strength of the opals.

Here, we present a fast, reliable, and accurate procedure to create 2D inorganic defect layers in artificial opals while still preserving the photonic strength of the lattice. The planar defect is formed by small aggregates of nanocrystalline colloids and can be made from a wide variety of materials. Accurate control of the defect thickness can be achieved, which yields control over the spectral position of the defect state introduced in the pseudogap of the colloidal crystal. This defect mode causes the opening of a narrow higher transmission window that can be accurately tuned during the synthesis.

Figure 1 displays a diagram of the procedure employed to build up the colloidal heterostructures. A suspension containing oxide crystallites is deposited and spun onto a planarized self-assembled colloidal crystal in order to create a uniform nanocrystalline slab on top of it (panels i–iv in Fig. 1). The subsequent growth of a new colloidal crystal on top of the nanocrystalline layer gives rise to a heterostructure, wherein the translational symmetry is disrupted by the presence of the slab (panels v and vi in Fig. 1).

The importance of control over the aggregation state of the nanoparticle suspension, as well as the wettability of the colloidal crystal by this suspension, is exemplified in Figure 2. In Figure 2 we show heterostructures obtained after carrying out the coating processes indicated in Figure 1 for three different types of nanocolloids, each having a different stability in suspension. Specifically, we have employed an aqueous suspension of silica nanoparticles (Ludox), a suspension of nanocrystalline titania in which different dispersants are present (HT Solaronix, see Experimental), and a suspension of ceria crystallites prepared in our laboratories in a solution of ethanol and water. Let us first focus on the effects of aggregation. Basically, the aggregates must be large enough to be prevented

[*] Dr. H. Míguez, Dr. R. Pozas, A. Mihi, Dr. M. Ocaña
Instituto de Ciencia de Materiales de Sevilla (CSIC-US)
Avenida Américo Vespucio s/n, Isla de La Cartuja
41092 Sevilla (Spain)
E-mail: hernan@icmse.csic.es

[**] This work has been funded by Fundación Ramón Areces. We thank F. Varela for his help during SEM characterization.

© 2006 WILEY-VCH Verlag GmbH & Co. KGaA, Weinheim

ADVANCED MATERIALS

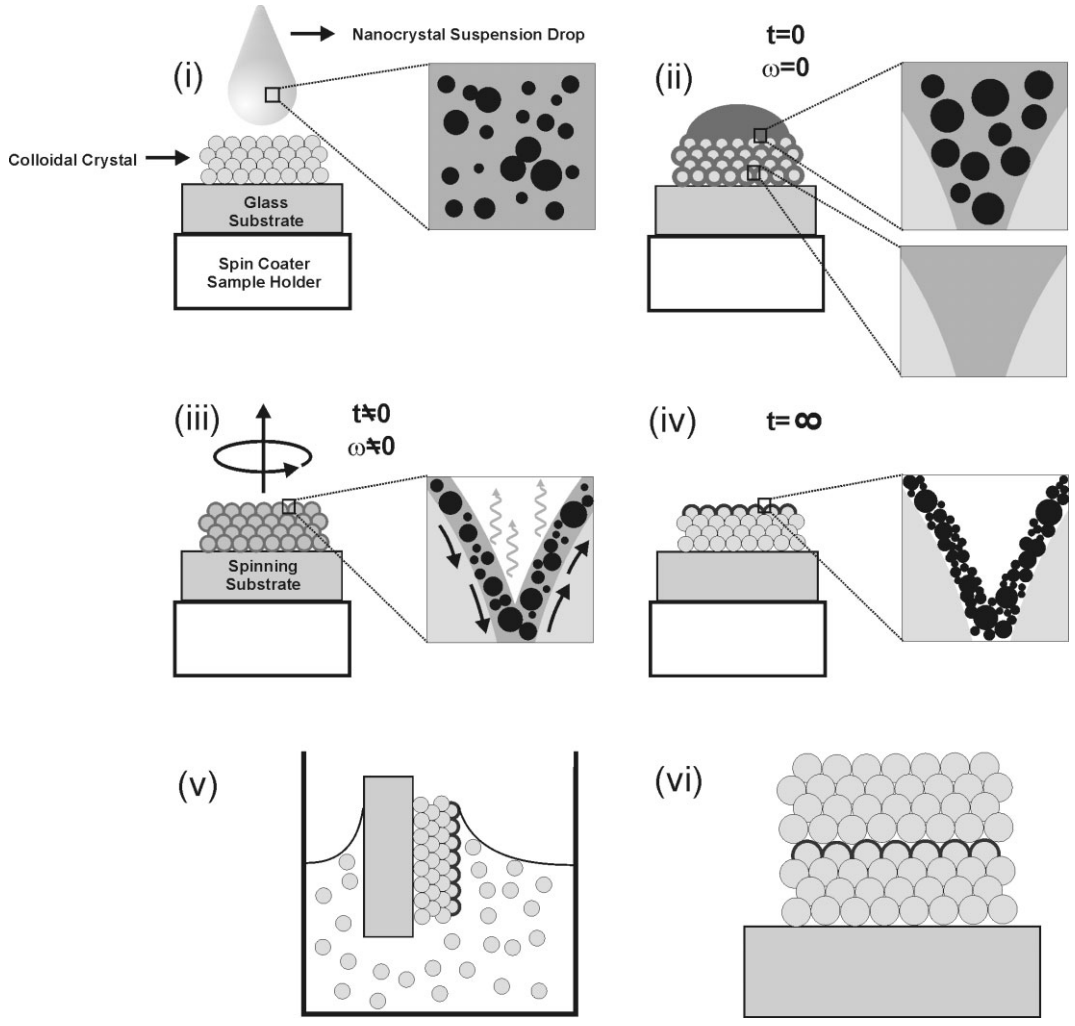

Figure 1. Scheme of the procedure employed to build up a nanocrystalline slab within a colloidal crystal. i) A suspension containing oxide crystallites is deposited onto a planar colloidal crystal. ii) A drop of the nanoparticle suspension is manually spread on the surface, causing the liquid medium to infiltrate the lattice at the same time. iii) The substrate is spun until all the solvent is evaporated, and iv) a uniform nanocrystalline slab is deposited on top of the substrate. v) Subsequent growth of a new colloidal crystal on top of the nanocrystalline layer gives rise to vi) a heterostructure in which the translational symmetry is disrupted by the presence of the slab.

from entering the opal-like structure through the external pores, but small enough to allow the formation of a smooth coating of controllable thickness on the colloidal lattice. The aggregate size distributions for very dilute suspensions of the three kinds of nanoparticles employed are shown in Figure 2a. Although in all cases the average size (l) of the nanoparticles is on the order of 10 nm, as measured by high-resolution electron microscopy, aggregation, caused either by chemical bonding or flocculation, gives rise to a very different final average cluster size ($\langle d \rangle$) for the titania and ceria crystallite suspensions ($\langle d \rangle \approx 160$ nm). On the other hand, the colloidal-crystal films employed in this work have been formed using $D = 720$ nm diameter polystyrene (PS) spheres. The size of the entrance windows, w, is estimated to be the diameter of the sphere that fits exactly between three spheres in the most external close-packed (111) plane of the lattice, as shown schematically in Figure 2b; this corresponds to $w = 0.1547 \times D$ (in our case, $w \approx 110$ nm). The scanning electron microscopy (SEM) images in Figures 2c–f clearly show the crucial role of the ratio $\langle d \rangle / w$. For Ludox nanocolloids ($w \gg \langle d \rangle = l$), the colloidal crystal substrate is infiltrated during the spin-coating process, making the structure useless for our present purpose (see Figs. 2c and d). For TiO_2 nanocrystalline aggregates ($w \approx \langle d \rangle > l$), a smooth and highly uniform capping layer is obtained, allowing for the subsequent formation of a high-quality colloidal crystal on it (Figs. 2e and f). Regarding wettability and adhesion, the case of the CeO_2 suspensions illustrates well the importance of these other key parameters. As can be seen in Figure 2a, for CeO_2 we have $w \approx \langle d \rangle > l$, similar to the situation with TiO_2. However, no coating is formed on the colloidal lattice after several attempts using a wide range of spinning velocities. Gradual substitution of the initial aqueous medium with ethanol finally results in the formation of a CeO_2 coating on the colloidal lattice, which only occurs when the

 © 2006 WILEY-VCH Verlag GmbH & Co. KGaA, Weinheim

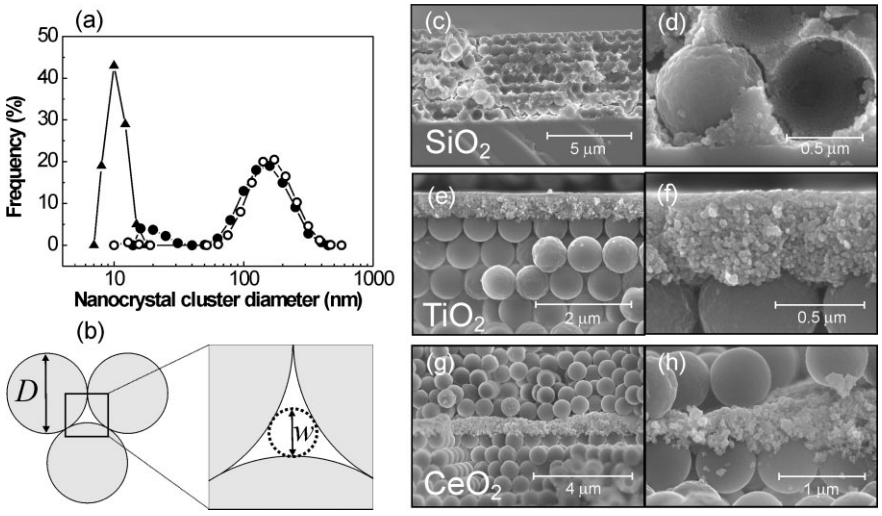

Figure 2. a) Analysis of the aggregation state of the nanoparticle suspensions employed. The size distribution is shown as the volume percentage of every cluster size found in suspension for SiO_2 (▲), TiO_2 (●), and CeO_2 (○) particles. b) Schematic representation of the shape of the external surface pores of the colloidal crystal and the diameter (w) of the equivalent circular entrance window. c–h) Low- and high-magnification scanning electron microscopy images of cross sections of colloidal crystals onto which different types of nanoparticles are deposited, specifically, c,d) SiO_2, e,f) TiO_2, and g,h) CeO_2; each image shows a different aggregation state.

medium contains 80 wt % alcohol. However, this improvement is accompanied by an increase of the aggregate size, giving rise to a rougher coating than in the case of TiO_2, which thus prevents the growth of a well-ordered upper crystal (Figs. 2g and h).

The uniform thickness of the deposited nanocrystalline-TiO_2 layer allows a new colloidal crystal to be grown on it by the vertical deposition method. Low-magnification scanning electron microscopy (SEM) analysis of cross sections of cleaved samples, as shown in Figures 3a and c, confirms that the quality of the upper lattice is similar to the lower one. Control over the thickness of the defect slab can be achieved by varying the spinning velocity, as seen in the high-magnification cross sections shown in Figures 3b and d (120 and 80 revolutions per second (rps), respectively), as well as in Figures 2e and f (40 rps). The deposited films are always in conformal contact with the bottom crystal, and are therefore corrugated at their lower face. Furthermore, for thin films, this corrugation is also present on the upper side, as seen in Figure 3b. Thus, a rough estimate of the defect thickness (T) can be extracted from the SEM images, and a more precise value is obtained by fitting the optical properties of the doped samples, as discussed in detail later. In Figure 3e we have plotted the observed dependence of the estimated thickness (T) of the deposited nanocrystalline titania layer with the spinning velocity. Interestingly, the data cannot be adequately fitted to a power law of the form $T \sim \omega^{-b}$, which is the dependence observed for all films made by spin-coating reported up to now, with empirical values of the exponent b typically around 0.5 for dilute polymers or glass precursors.[20] Besides, in our case, the plot of T versus ω shows an abrupt change in the thinning rate at around 80–100 rps. These anomalous effects may have their origin in the fact that our spin-coating process is performed using a colloidal crystal as the substrate. First, the liquid phase of the crystallite suspension is removed not only by evaporation due to the fast spinning speed, but also can be soaked up by the porous substrate. The kinetics of this process may differ from that observed when spinning a thin film onto a dense wafer, resulting in deviations from power law behavior. Secondly, unlike most spin-coated films, our nanocrystalline-TiO_2 layer is deposited onto a periodically corrugated surface, which will also affect how it spreads. In fact, a series of coatings made using $\omega = 100$, 120, and 140 rps preserve the corrugation of the colloidal lattice surface, as shown by Figure 3b. For thicker defect layers (i.e., at lower spinning speeds), however, this inherited corrugation is greatly smoothed out, as can be seen in Figures 2f and 3d. This change in the corrugation of the upper face of the deposited nanocrystalline film occurs in the same range of ω at which the thinning rate of the T versus ω curves changes. SEM images shown as insets to Figure 3e illustrate the typical shapes of films obtained using speeds located at two ends of the range under analysis. Therefore, the corrugation seems to hinder the spreading of the nanoparticles in the forming film, resulting in a slower growth rate than observed for thicker films.

The nanocrystalline defect layer behaves as an optical dopant, causing the opening of well-defined allowed state bands within the forbidden frequency interval of the surrounding lattice. In our case, these are detected as narrow dips in the spectral range at which the (111) Bragg reflection is observed. Vertical dotted lines point out the position of such dips in the reflectance spectra shown in Figure 4. Curves in Figures 4a–c correspond to differently doped samples, each built using a different spinning velocity to deposit the defect layer. Curves calculated using a scalar wave approximation are shown as thin lines superimposed on the experimental plots.[21] It should be noted that the dip induced by the presence of the defect at pseudogap frequencies shows a reflectance value close to the value predicted by theory.[22] This implies a clear improvement with respect to previously reported colloidal crystals containing planar defects made by CVD of metal oxides.[16,17] In that case, the Q-factor of the cavity was greatly diminished, either by the low photonic strength of the infiltrated host lattice or by imperfections introduced during the inversion process. In the approach presented here, the nanocrystalline middle layer is deposited without altering the composition of the lattice, hence maintaining its photonic strength. Interestingly, while good fittings are obtained for the

 © 2006 WILEY-VCH Verlag GmbH & Co. KGaA, Weinheim

ADVANCED MATERIALS

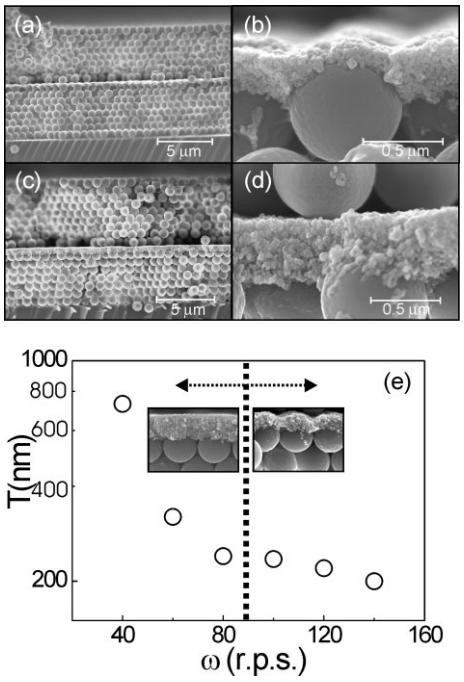

Figure 3. SEM images of the cross sections of two colloidal crystals made from spheres of the same size (average diameter of around 700 nm) with embedded nanocrystalline-TiO_2 slabs of two different thicknesses, resulting from two different spinning speeds employed during the fabrication process, specifically, a,b) 120 rps and c,d) 80 rps. e) The graph shows the variation of the effective thickness (*T*) of the nanocrystalline film deposited on the colloidal crystal, as estimated from the optical properties, versus the spinning speed of the substrate. The SEM images introduced as insets serve as examples of the different film shapes obtained at the lower and higher speed ends of the range employed here.

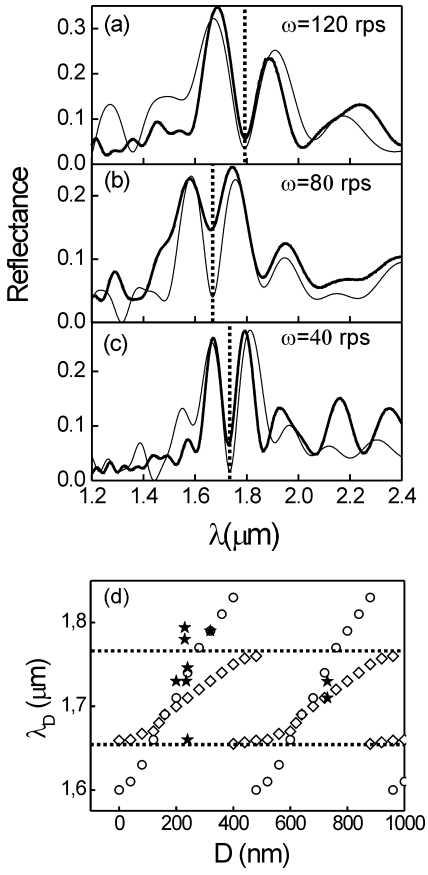

Figure 4. a–c) Thick solid lines correspond to the specular reflectance spectra of three colloidal lattices containing nanocrystalline-TiO_2 planar defects deposited employing different spinning speeds: a) 120 rps, b) 80 rps, and c) 40 rps. The average diameter of the PS spheres is 720 nm in all cases. The crystal size changes slightly from sample to sample. Structural parameters extracted from the SEM characterization are introduced in the calculations to obtain the simulated spectra (shown as thin solid lines) in each case. An estimation of the effective planar defect thickness is obtained by fitting both the dip position and shape at the pseudogap frequencies in each case. d) The experimental variation of the dip position λ_D associated with the defect state, and thus the nanocrytalline-TiO_2 layer thickness, are shown (★). The theoretical dependence between λ_D and *T* for a planar defect sandwiched between two 5 (○) and two 50 (◇) sphere monolayer lattices is also shown.

optical features observed at energies corresponding to the dielectric band and the pseudogap regions, the properties observed at air band frequencies cannot be simulated properly. This is clearly in contrast with previous simulations of the optical properties of colloidal crystals containing planar defects using the scalar wave approximation, wherein excellent fits were obtained for the entire reflectance spectrum.[17] The origin of this difference may arise from the fact that the 2D defect we have built by spin-coating is not symmetric as in the previous case, since its upper and lower faces present a different corrugation.

By changing the angular speed of the spin-coater, which controls the thickness of the defect layer, the defect state position can be shifted. Both the calculated and the experimentally observed variation of the spectral position of the transmission window at pseudogap frequencies with the thickness of the nanocrystalline-TiO_2 defect are plotted in Figure 4d. Theoretical results obtained using the scalar wave approximation are shown for defects embedded within very thin lattices (5 monolayers each, circles) and for thick ones (50 monolayers each, diamonds) to illustrate the strong interplay between finite crystal size effects and those related to the presence of a defect. Defect slabs of similar thickness may give rise to different intra-gap states depending on the width of the crystals surrounding it. Most of the experimental data, plotted as stars in Figure 4d, fall in between the theoretical curves obtained for the two crystal sizes considered. As reported before,[17] the planar defect state sweeps the Bragg peak full-width from the blue to the red end as the thickness of the defect increases, and repeats this behavior cyclically. For thinner crystals, the Bragg peak broadens, and therefore it is possible to obtain planar cavity modes at frequencies outside the stop band limits of the infinite crystal, depicted as horizontal dotted lines in Figure 4d.

In conclusion, we have developed a method to introduce planar defects with nanocrystalline structure inside colloidal crystal films. Such defects are spun in minutes, without diminishing either the lattice quality or photonic strength of the crystal. Well-defined optical reflectance dips at pseudogap

 © 2006 WILEY-VCH Verlag GmbH & Co. KGaA, Weinheim

frequencies confirm the improvement with respect to previous techniques employed to dope this type of photonic crystals. We have also demonstrated that the spectral position of the defect states can be tuned by the size of the defect layer, which is controlled by the rotation speed of the substrate during the spin-coating process. We foresee that these optical materials might have applications in fields in which nanoparticulate materials are used as photochemically active compounds, such as photocatalysis or dye-sensitized photovoltaics.

Experimental

Fabrication of Colloidal Crystal Films: The growth of colloidal crystals from PS colloids in deionized water was carried out using a variation of the vertical-deposition method developed by Colvin and coworkers [4]. For this purpose, commercial PS colloidal particles (IKERLAT) with an average diameter of 720 nm (polydispersity of about 3 %) were used. The substrates employed were glass microscope slides (12 mm × 76 mm), which were cleaned with doubly distilled water, acetone, carbon tetrachloride, and with a 4:1 (v/v) H_2SO_4/H_2O_2 solution before being dried under a N_2 flow. These substrates were then dipped into a cylindrical glass beaker (inner diameter: ~ 25 mm; volume: 25 mL) containing the PS colloidal suspensions (15 mL) with a concentration of 0.04 wt %. Subsequently, the beakers were placed in an oven at 50 °C and water was evaporated at a rate of 0.22 mm h^{-1} for 3 days, resulting in the formation of a high-quality colloidal crystal on a 12 mm × 16 mm area of the substrate.

Nanocrystal Preparation: Commercial SiO_2 nanoparticles (size of ~ 15 nm, TMA Ludox particles, DuPont product, suspension in deionized water) or TiO_2 nanocrystals (size of ~ 13 nm, Solaronix HT, suspension in a mixture of water, ethanol, and polyethylene oxide) were used as received. CeO_2 nanocrystals (size of ~ 12 nm) were synthesized by homogeneous precipitation by aging a 0.005 mol dm^{-3} Ce(III) nitrate aqueous solution in the presence of 0.05 mol dm^{-3} hexamethylenetetramine at 100 °C for 2 h, following a method described elsewhere [23]. Nanoparticle aggregate size measurements were carried out by photocorrelation spectroscopy employing a Malvern ZetaMaster apparatus.

Nanocrystalline Defect Layer Preparation: In order to deposit uniform layers of nanocrystals on the lattice surface, colloidal suspensions of such particles were prepared in water (40 g L^{-1} for SiO_2 and 85 g L^{-1} for TiO_2) or ethanol/water mixtures (50 g L^{-1} for CeO_2). Then, 30 μL of the resulting suspension was added to a glass slide on which an opal film had been deposited as previously described, and spun immediately at a constant velocity using a desktop spin-coater (Novocontrol) for 2 min. The coating thickness was controlled by modifying the spin velocity in the 40 to 140 rps range. Finally, in order to grow a new colloidal crystal of latex on top of the inorganic capping, the colloidal crystal growth procedure described above was employed again but with a PS particle concentration of 0.075 wt % instead of 0.04 wt %. Since the second crystal was grown on a different substrate (nanocrystalline-TiO_2 instead of a glass substrate), the suspension–substrate surface tension changed and a different concentration was needed in order to achieve a similar crystal size. Micrographs of cross sections of the different samples were obtained using a Hitachi S5200 field-emission SEM.

Optical Spectroscopy: Optical characterization was performed using a Fourier transform infrared spectrophotometer (Bruker IFS-66) attached to a microscope, operating both in reflection and transmission mode. For reflectance measurements, an X4 objective with a numerical aperture of 0.1 (light cone angle of ± 5.7°) was used to irradiate the sample and collect the reflected light at quasi-normal incidence with respect to the (111) planes of the colloidal lattice. A spatial filter was used to selectively detect light from 0.1 mm^2 circular regions of the sample.

Simulated Spectra: The optical specular reflectance results were fitted using spectra generated by a Mathematica code based on a scalar wave approximation, as described previously by others [22]. Structural data employed to simulate the spectra shown in Fig. 4 are detailed next. Spectrum a, corresponding to $\omega = 120$ rps: top crystal thickness was $t_C = 5$ sphere monolayers; defect layer (variable parameter) thickness was $T = 220$ nm; bottom crystal thickness $t_{C2} = 6$ monolayers. Spectrum b, $\omega = 80$ rps: $t_C = 7$ monolayers; $T = 240$ nm; $t_{C2} = 6$ monolayers. Spectrum c, corresponding to $\omega = 40$ rps: $t_C = 7$ monolayers; $T = 720$ nm; $t_{C2} = 7$ monolayers. The refractive index of the spheres was assumed to be 1.59 (PS). The refractive index of the defect slab was assumed to be 1.75, since nanocrystalline-TiO_2 layers typically have a porosity of 50 % [24].

Received: October 21, 2005
Final version: December 14, 2005

[1] E. Yablonovitch, T. J. Gmitter, R. D. Meade, A. M. Rappe, K. D. Brommer, J. D. Joannopoulos, *Phys. Rev. Lett.* **1991**, *67*, 3380.
[2] J. D. Joannopoulos, P. R. Villeneuve, S. Fan, *Nature* **1997**, *386*, 143.
[3] Y. A. Vlasov, V. N. Astratov, A. V. Baryshev, A. A. Kaplyanskii, O. Z. Karimov, M. F. Limonov, *Phys. Rev. E: Stat. Phys., Plasmas, Fluids, Relat. Interdiscip. Top.* **2000**, *61*, 5784.
[4] P. Jiang, J. F. Bertone, K. S. Hwang, V. L. Colvin, *Chem. Mater.* **1999**, *11*, 2132.
[5] Y. A. Vlasov, X. Z. Bo, J. C. Sturm, D. J. Norris, *Nature* **2001**, *414*, 289.
[6] S. Wong, V. Kitaev, G. A. Ozin, *J. Am. Chem. Soc.* **2003**, *125*, 15 589.
[7] S. M. Yang, H. Míguez, G. A. Ozin, *Adv. Funct. Mater.* **2002**, *12*, 425.
[8] W. Lee, S. A. Pruzinsky, P. V. Braun, *Adv. Mater.* **2002**, *14*, 271.
[9] N. Tetreault, H. Míguez, S. M. Yang, V. Kitaev, G. A. Ozin, *Adv. Mater.* **2003**, *15*, 1167.
[10] B. H. Juarez, D. Golmayo, P. A. Postigo, C. López, *Adv. Mater.* **2004**, *16*, 1732.
[11] F. Jonsson, C. M. Sotomayor Torres, J. Seekamp, M. Schniedergers, A. Tiedemann, J. Ye, R. Zentel, *Microelectron. Eng.* **2005**, *429*, 78.
[12] E. Vekris, V. Kitaev, G. von Freymann, D. D. Perovic, J. S. Aitchison, G. A. Ozin, *Adv. Mater.* **2005**, *17*, 1269.
[13] Q. F. Yan, Z. C. Zhou, X. S. Zhao, S. J. Chua, *Adv. Mater.* **2005**, *17*, 1917.
[14] Y. H. Jun, C. A. Leatherdale, D. J. Norris, *Adv. Mater.* **2005**, *17*, 1908.
[15] Y. Zhao, K. Wostyn, G. de Schaetzen, K. Clays, L. Hellemans, A. Persons, M. Szekeres, R. A. Schoonheydt, *Appl. Phys. Lett.* **2003**, *82*, 3764.
[16] E. Palacios-Lidon, J. F. Galisteo-Lopez, B. H. Juarez, C. Lopez, *Adv. Mater.* **2004**, *16*, 341.
[17] N. Tetreault, A. Mihi, H. Miguez, I. Rodriguez, G. A. Ozin, F. Meseguer, V. Kitaev, *Adv. Mater.* **2004**, *16*, 346.
[18] H. Míguez, N. Tetreault, B. Hatton, S. M. Yang, D. Perovic, G. A. Ozin, *Chem. Commun.* **2002**, 2736.
[19] N. Tétreault, A. C. Arsenault, A. Mihi, S. Wong, V. Kitaev, I. Manners, H. Míguez, G. A. Ozin, *Adv. Mater.* **2005**, *17*, 1912.
[20] D. Meyerhofer, *J. Appl. Phys.* **1978**, *49*, 3993.
[21] a) S. Satpathy, Z. Zhang, M. R. Salehpour, *Phys. Rev. Lett.* **1990**, *64*, 1239. b) K. W. K. Shung, Y. C. Tsai, *Phys. Rev. B: Condens. Matter Mater. Phys.* **1993**, *48*, 11 265.
[22] The scalar wave approximation has been repeatedly employed to successfully fit the optical properties of colloidal crystals and complex architectures built based on them. Examples of its application to colloidal crystals can be found in the following references: a) D. M. Mittleman, J. F. Bertone, P. Jiang, K. S. Hwang, V. L. Colvin, *J. Chem. Phys.* **1999**, *111*, 345. b) P. Jiang, G. N. Ostojic, R. Narat, D. M. Mittleman, V. L. Colvin, *Adv. Mater.* **2001**, *13*, 389. c) G. von Freymann, S. John, S. Wong, V. Kitaev, G. A. Ozin, *Appl. Phys. Lett.* **2005**, *86*, 053 108. d) A. Mihi, H. Míguez, *J. Phys. Chem. B* **2005**, *109*, 15 968.
[23] T. C. Rojas, M Ocaña, *Scr. Mater.* **2002**, *46*, 655.
[24] M. Grätzel, *Prog. Photovolt. Res. Appl.* **2000**, *8*, 171.

© 2006 WILEY-VCH Verlag GmbH & Co. KGaA, Weinheim